



Nanoscale

**Transition-metal single atoms embedded into defective BC3
as efficient electrocatalysts for oxygen evolution and
reduction reactions**

Journal:	<i>Nanoscale</i>
Manuscript ID	NR-ART-10-2020-007580.R1
Article Type:	Paper
Date Submitted by the Author:	07-Dec-2020
Complete List of Authors:	Zhou, Yanan; Sichuan University, School of Chemical Engineering; Lawrence Berkeley National Laboratory, Materials Science Division Gao, Guoping; Lawrence Berkeley National Laboratory, Berkeley, Chu, Wei; Sichuan University (Top 12th Univ in China), Dept Chemical Engineering Wang, Lin-Wang; Lawrence Berkeley National Laboratory,

SCHOLARONE™
Manuscripts

Transition-metal single atoms embedded into defective BC₃ as efficient electrocatalysts for oxygen evolution and reduction reactions

Yanan Zhou,^{a,b} Guoping Gao,^b Wei Chu,^{*a} and Lin-Wang Wang^{*b}

^aSchool of Chemical Engineering, Sichuan University, Chengdu, 610065, Sichuan, China

^bMaterials Science Division, Lawrence Berkeley National Laboratory, Berkeley, 94720, California, United States

*Corresponding authors.

E-mail address: chuwei1965@scu.edu.cn (Wei Chu); lwwang@lbl.gov (Lin-Wang Wang).

Abstract

Searching for high-activity, stable and low-cost catalyst toward oxygen evolution reaction (OER) and oxygen reduction reaction (ORR) is of significant importance to the development of renewable energy technologies. By using the computational screening method based on density functional theory (DFT), we have systematically studied a wide range of transition metal (TM) atoms doped defective BC₃ monolayer (B atom vacancy V_B and C atom vacancy V_C), denoted as TM@V_B and TM@V_C (TM = Mn, Fe, Co, Ni, Cu, Ru, Rh, Pd, Ir and Pt), as efficient single atom catalysts for OER and ORR. The calculated results show that all the considered TM atoms can tightly bind with the defective BC₃ monolayers to prevent the atomically dispersed atoms from clustering. The interaction strength between intermediates (HO*, O* and HOO*) and catalyst govern the catalytic activities of OER and ORR, which demonstrated has a direct correlation with the *d*-band center (ϵ_d) of TM active site that can be tuned by adjusting TM atoms with various *d* electron numbers. For TM@V_B catalysts, it was found that the best catalyst for OER is Co@V_B with an overpotential η^{OER} of 0.43 V followed by Rh@V_B ($\eta^{\text{OER}} = 0.49$ V), while for ORR, Rh@V_B exhibits the lowest overpotential η^{ORR} of 0.40 V followed by Pd@V_B ($\eta^{\text{ORR}} = 0.45$ V). For TM@V_C catalysts, the best catalyst for OER is Ni@V_C ($\eta^{\text{OER}} = 0.47$ V) followed by Pt@V_C ($\eta^{\text{OER}} = 0.53$ V), and for ORR, Pd@V_C

exhibits the highest activity with η^{ORR} of 0.45 V. The results suggest that the high activity of the newly predicted well dispersed Rh@V_B SAC is comparable to those of noble metal oxides benchmark catalysts for both OER and ORR. Importantly, Rh@V_B may remain stable against dissolution at pH = 0 condition. The high energy barrier prevents the isolated Rh atom from clustering and ab initio molecule dynamic simulation (AIMD) result suggests that Rh@V_B can remain stable under 300 K, indicating its kinetic stability. Our findings highlight a novel family of efficient and stable SAC based on carbon material, which offers a useful guideline to screen the metal active site for catalyst designation.

Introduction

The development of sustainable and renewable energy technologies, such as water splitting, fuel cells, and metal-air batteries, have attracted tremendous attention due to the growing global energy crisis and serious environmental pollution problems^[1-3]. To realize these technologies, two electrochemical energy conversion processes are at the core: the anodic oxygen evolution reaction of electrochemical water splitting cell with Ru/Ir oxides^[1, 4, 5] as the most advanced catalysts; however, as a reverse reaction of OER, the cathodic oxygen reduction reaction of the fuel cell and metal-air battery with Pt oxides and its alloys^[6, 7] as the most active ORR catalysts. However, the sluggish kinetics of OER and ORR limit their overall energy conversion efficiency even for these noble metal catalysts. Furthermore, the scale-up applications of these renewable energy technologies will be greatly restricted unless the scarce and expensive noble metal oxides catalysts can be replaced by other low-cost yet efficient electrodes^[8, 9]. The recent researches of using single metal atom doped on two-dimensional (2D) materials open up a new revenue method for searching the alternative catalysts^[10-14]. Single-atom catalysts (SACs) which can promise the maximum atom-utilization efficiency and provide the tunable number of active sites have been extensively investigated theoretically and experimentally since the work of Pt₁/FeO_x SAC was reported by Zhang *et al*^[15]. However, the increasing surface free energy as the size of metal particles decrease to single atoms will result in metal aggregation^[16]. Therefore, to maintain the excellent catalytic properties of SACs and use reasonable metal resources, it is vital to search for appropriate support to anchor the isolated atoms steadily and against

aggregation.

Sparked by the discovery of graphene^[17], 2D materials possessing sheet-like structures with only single- or few-atom thickness have been experimentally realized widely, which has attracted intensive interest in exploring the novel properties and potential applications of these unique 2D materials^[18, 19], especially in the research area of SACs^[20, 21]. To date, different carbon-based supports for SACs as electrocatalysts have intensively increased owing to their low-cost, high catalytic performance and long-term stability^[22], such as modified graphene^[23-28], g-C₃N₄^[29], metal-organic frameworks^[30, 31], graphdiyne^[32, 33] and phthalocyanine^[34, 35]. Boron atoms are normally used as the dopants in carbon materials. The 2D allotropes of different boron doped carbon sheets were studied both experimentally and theoretically^[25, 36, 37]. The novel BC₃ honeycomb sheet with excellent crystalline quality was grown uniformly on a macroscopic surface area of NbB₂ (0001) in an epitaxial way, which was demonstrated to be a monolayer film^[38]. Many experimental and theoretical studies have been done to investigate the structural and electronic properties of 2D BC₃ since its successful synthesis^[39-41]. BC₃ monolayer have been demonstrated to be potential anode materials for batteries^[42, 43]. Monolayer BC₃ and its derivatives have also been predicted to be suitable for gas sensor and capture^[44, 45]. Meanwhile, Ni *et al.* found that the doped BC₃ with transition metal atoms have the potential applications in electronic and spintronic devices^[46, 47]. All above previous works indicate that the experimentally available BC₃ monolayer can be as excellent potential substrates for catalysts. Nevertheless, so far, a systematic theoretical investigation on the using of BC₃ monolayer as the substrate for SACs toward electrochemistry is lacking. Such theoretical study is vital and necessary given the tremendous speed of progress in the experimental work in this field. However, the interaction strength between pristine BC₃ monolayer and TM atoms is weak that make them easy to aggregate into clusters^[48]. Defects can significantly affect the properties of nanomaterials^[49, 50]. In the experiments, defects can be deliberately introduced by irradiation or chemical treatments on carbon-based materials^[49]. The introducing vacancies can serve as the active sites bind with TM atoms^[51].

In this work, five 3*d* metals (Mn, Fe, Co, Ni, and Cu), three 4*d* metals (Ru, Rh, and Pd), and two 5*d* metals (Ir and Pt) were chosen to construct transition metal atoms doped defective

BC₃ monolayer catalysts, as these metals are commonly used to design SACs for OER and ORR. The scaling relationship among the adsorption Gibbs free energies of the OER/ORR intermediates is used to describe the catalytic activity trend. The dissolution possibility of the designed SACs was also considered to check its stability under the catalytic conditions.

Computational methods

All the calculations were performed by the Vienna ab initio Simulation Package (VASP) code^[52, 53] using spin-polarized density functional theory (DFT) method. The projector augmented wave (PAW) pseudopotentials were used to describe the nuclei–electron interactions^[54]. The Perdew-Burke-Ernzerhof (PBE)^[55] exchange–correlation functional of the generalized gradient approximation (GGA)^[56] was used to describe the electron interactions. The van der Waals (vdW) effect was described using the Grimme’s DFT-D3 correction method^[57]. A plane-wave cutoff energy of 500 eV was adopted for all the computations to describe all atoms’ valence electrons. Geometry optimizations were performed until the force on each atom is less than 10⁻² eV Å⁻¹. The energy was converged to be less than 10⁻⁵ eV. A vacuum space of 20 Å was used to avoid the interaction between the periodic images. The Monkhorst-Pack grid^[58] in the Brillouin zone with a mesh grid of 3x3x1 was sampled for the structural optimization, and the Bader charge analysis was performed to evaluate the charge transfer process^[59]. The diffusion barrier was calculated by using the climbing image nudged elastic band (CINEB) method^[60, 61]. Considering the effect of polarization due to the water condition on OER and ORR, we used the implicit water solvent model with VASPsol throughout all the calculations^[62]. The details of OER and ORR calculations are shown in the supporting information as in our previous work^[12]. The adsorption Gibbs free energy is defined as the following equation (1):

$$G_{\text{ads}} = G_{\text{adsorbent+catalyst}} - G_{\text{catalyst}} - G_{\text{adsorbent}} \quad (1)$$

Here, $G_{\text{adsorbent+catalyst}}$, G_{catalyst} , and $G_{\text{adsorbent}}$ refer to the Gibbs free energy of adsorbent on catalyst, isolated catalyst, and isolated adsorbent, respectively.

Results and discussion

As shown in **Fig. S1** in the Supporting Information, the unit cell of the BC₃ sheet consists of

six C and two B atoms. The bond length of C-C and C-B in unit cell are 1.42 Å and 1.56 Å, respectively, and the optimized crystal lattice parameter of BC₃ is 5.17 Å, which are in line with the previous literatures^[63, 64]. A 3x3x1 supercell was used to model the TM-doped BC₃ monolayer. There are two types of the monovacancy in BC₃ monolayer, one is B monovacancy (V_B) by removing a single B atom, and the other one is C monovacancy (V_C) by removing a single C atom from the BC₃ monolayer. There are two types of double vacancies in the BC₃ monolayer: one is vacancy BC (V_{BC}) created by removing one B atom and its neighboring N atom; the other one is vacancy CC (V_{CC}) obtained by removing two neighboring C atoms. The optimized structures for the pristine-BC₃ (p-BC₃), V_B, V_C, V_{BC} and V_{CC} are shown in **Fig. S1a-e**, respectively. For V_B, the C-C and C-B bond lengths near the vacancy are shortened to 1.37 and 1.54 Å, respectively. It causes the carbon atoms to move away from the vacancy area, and the distance between them increases from 2.71 Å in the p-BC₃ to 2.81 Å in the V_B. Since the stretch of the bond length, there is no Jahn-Teller distortion occurring in the V_B. For V_C, there is also no significant structural reconstruction around the vacancy. The bond lengths of C-C and C-B in V_C near the vacancy are almost the same as those in the p-BC₃ monolayer. The nearest-neighboring atoms move toward the vacancy. The distances of these C-C and C-B are 2.50 and 2.59 Å, respectively. For V_{BC}, the C-B bond length near the vacancy is 1.64 Å, and the C-C bond lengths around the vacancy are 1.68 and 2.83 Å, respectively. For V_{CC}, the C-C and C-B bond lengths near the vacancy are about 1.43 and 1.81 Å, respectively. The vacancy formation energy (E_f) is an important physical parameter to describe the stability of the defects in BC₃ monolayer, and defined as $E_f = E_V - E_P + \mu_{\text{host}}$ ^[65, 66]. Here, E_V and E_P are the total energies of the defective and pristine BC₃ sheets, respectively. μ_{host} is the chemical potential of the removed atom (B or C), determined by the total energy per atom in pristine graphene or borophene, respectively. The computed E_f values for V_B, V_C, V_{BC} and V_{CC} are 5.42, 4.38, 7.21 and 5.95 eV, respectively, suggesting that the monovacancies (V_B and V_C) are thermodynamically favored over double vacancies (V_{BC} and V_{CC}). Compared to the formation energy of the single vacancy in graphene (7.45 eV)^[67], the much lower formation energies of the V_B and V_C suggest that their formation is thermodynamically more favorable. Thus, the following studies were based on the V_B and V_C. The calculated density of states (DOS) in **Fig. S1f-h** show that p-BC₃ monolayer is a

semiconductor with a band gap about 0.53 eV at the PBE level calculation, which agrees with previous results^[63]. V_B is a metallic sheet, whereas, V_C maintains semiconducting properties with the reduced band gap of 0.38 eV at the PBE level calculation, suggesting the better electric conductivity of V_B . Additionally, both of the mono vacancies V_B and V_C are nonmagnetic.

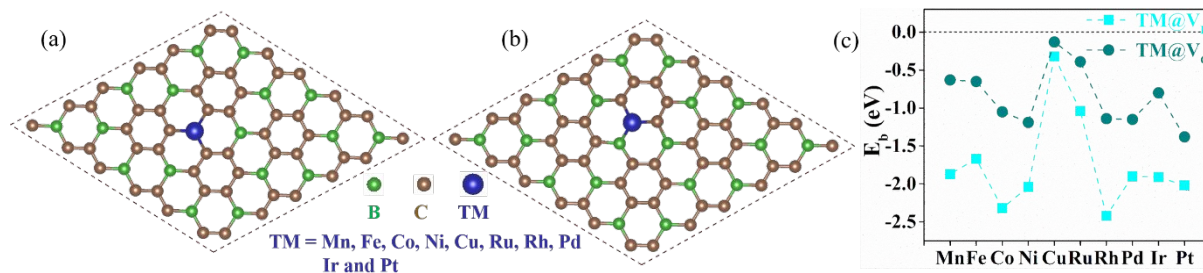


Fig. 1. (a) top view of TM@V_B monolayer, (b) top view of TM@V_C monolayer, and (c) binding energies of transition metals doped on the V_B and V_C systems.

To study the stability of the transition metal atoms doped V_B and V_C as the SACs, namely, TM@V_B and TM@V_C, we calculated their binding energies (E_b). The binding energy is defined as $E_b = E(\text{TM}@V_{C/B}) - E(\text{TM}) - E(V_{C/B})$, where $E(\text{TM}@V_{C/B})$ is the total energy of the TM@V_C or TM@V_B system, $E(V_{C/B})$ is the total energy of the V_C or V_B monolayer. $E(\text{TM})$ refers to the total energy of a metal atom in the corresponding most stable bulk crystal. The calculated results indicate that all the TM atoms prefer to be doped on the vacancy area for both V_B and V_C systems (**Fig. 1a and b**). The computed binding energies are shown in **Fig. 1c**, within which, all the negative value of E_b suggests that defective BC₃ monolayer can stabilize these doped TM atoms against clustering. The partial density of states (PDOS) in **Fig. 2 and 3** show that there exist hybridization between the 2p orbital of C/B and d orbital of TM, as well as between C-2p and B-2p orbitals on the TM@V_B and TM@V_C systems. The above results suggest that the interaction between TM atoms and V_B as well as V_C is strong, which can be further confirmed by the charge transfer during the TM atoms' binding process (**Table S1 and S2**). Additionally, the Bader charge analysis results indicate that the TM centers in all the considered catalysts are positively charged, suggesting that they can sever as the active sites to bind with intermediate species (HO*, O* and HOO*). The *d* band center is known as a descriptor to describe the interaction strength of the

adsorbate on the catalyst^[68, 69]. For all the TM@V_B and TM@V_C systems, it can be seen that ϵ_d move to lower energy with the increase of the *d*-orbital number of TM, suggesting that the interaction strength between reaction intermediate and catalyst is expected to have a similar trend with the previously calculated ϵ_d . This is indeed true from the calculated adsorption free energies of the reaction intermediates for OER and ORR (Fig. S2, Table S3 and S4).

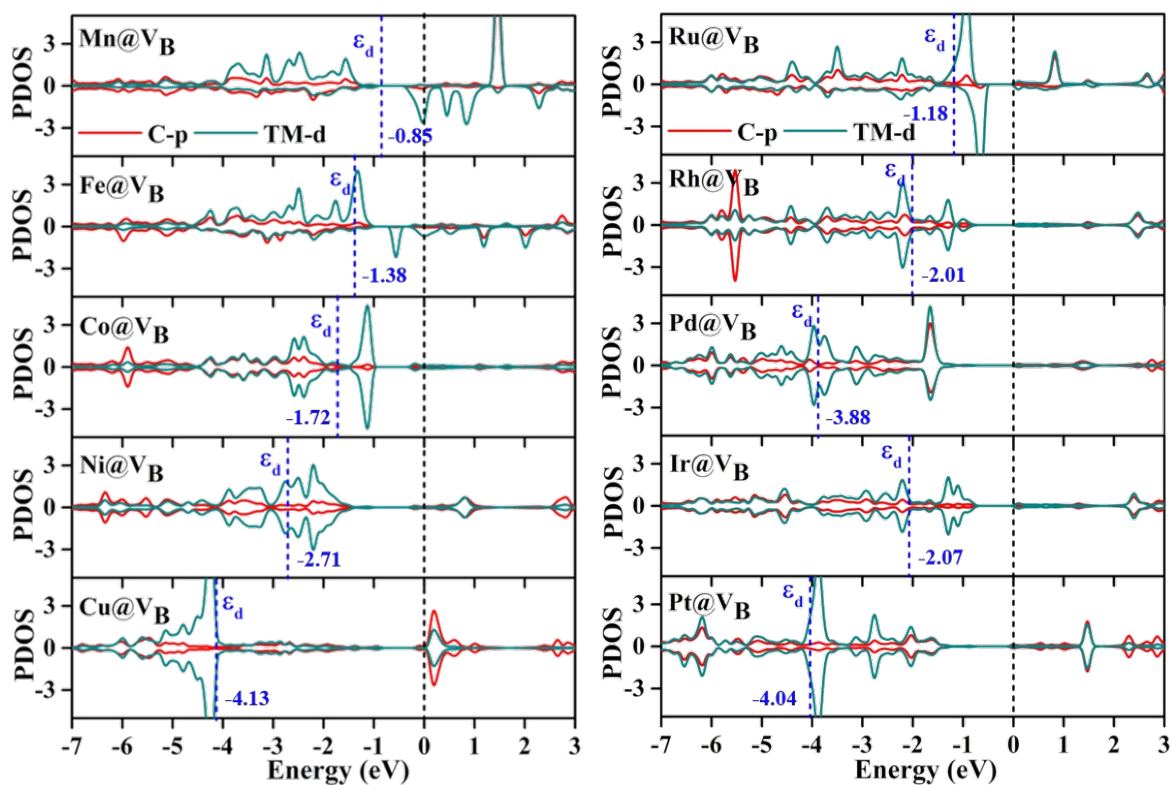


Fig. 2. Calculated PDOS of the TM@V_B systems. The Fermi level is set at zero (black dashed line) and the *d* band center (ϵ_d) and its corresponding value are marked by blue.

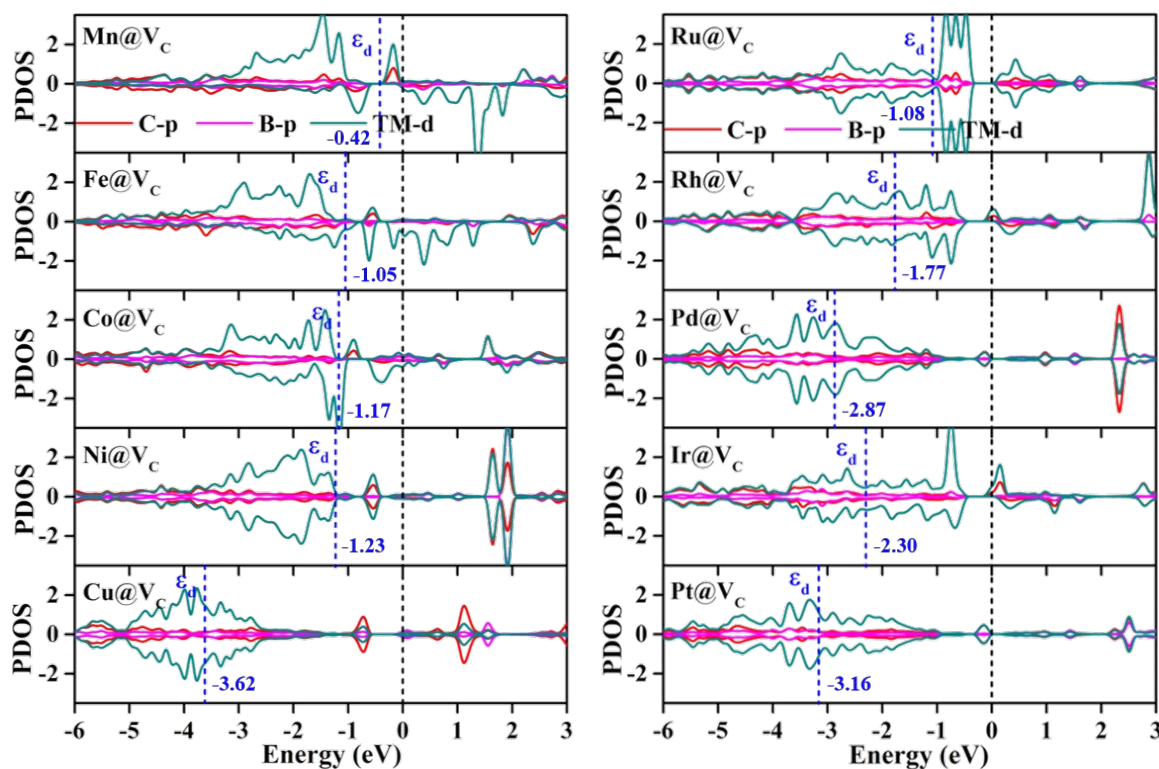


Fig. 3. Calculated PDOS of the TM@V_C systems. The Fermi level is set at zero (black dashed line) and the *d* band center (ϵ_d) and its corresponding value are marked by blue.

As proposed by Nørskov *et al*^[70], the adsorption Gibbs free energies of intermediates (ΔG_{HO^*} , ΔG_{O^*} , and ΔG_{HOO^*}) on catalyst govern the intrinsic catalytic activity toward OER and ORR. Thus, we calculated the adsorption Gibbs free energies of all the intermediates adsorbed on TM@V_B and TM@V_C catalysts and listed in **Table S3 and S4**. Our results show that the stable sites of intermediates on the catalysts are all at the top of TM atoms. Three descriptors, adsorption Gibbs free energy of adsorbed HO*, O* and HOO* were calculated to evaluate the catalytic activity and the rate-determining steps of OER/ORR. Sabatier's principle suggests that the adsorption energy of adsorbed intermediate on the catalyst should be neither too high nor too low due to both can lead to the adversarial effect on the catalytic activity^[71]. Thus, it is important to tune the moderate adsorption strength between the intermediate and catalyst as the promising electrocatalyst toward OER/ORR. As an ideal electrocatalyst at the $U = 0$ V condition, the values of ΔG_{HO^*} , ΔG_{O^*} and ΔG_{HOO^*} should be 1.23, 2.46 and 3.69 eV, respectively, with energy distances between two adjacent intermediate states for all the steps are equal to 1.23 eV. Therefore, OER and ORR can occur at their thermodynamic limitation and the corresponding overpotential η value is equal to 0

V. While, in fact, the energy distances between two adjacent intermediate states are not equal that result in the reaction limitations. The overpotential of OER (η^{OER}) is determined by the maximum energy distances of the two adjacent Gibbs free energies, while, the overpotential of ORR (η^{ORR}) is determined by the minimum energy distances of the two adjacent Gibbs free energies. Therefore, if the catalytic activity of an electrocatalyst has a correlation with the above three descriptors, it can provide us a route to rational design potential electrocatalyst via descriptor-based approach^[72, 73]. The scaling relationships of ΔG_{HO^*} vs ΔG_{HOO^*} and ΔG_{HO^*} vs ΔG_{O^*} for all the considered electrocatalysts are shown in **Fig. 4**. Obviously, for the TM@V_B systems (**Fig. 4a**), both ΔG_{HOO^*} and ΔG_{O^*} can be expressed as the function of ΔG_{HO^*} via equations $\Delta G_{\text{HOO}^*} = 0.84\Delta G_{\text{HO}^*} + 3.25$ and $\Delta G_{\text{O}^*} = 1.75\Delta G_{\text{HO}^*} + 1.22$, respectively. The relationship between ΔG_{HOO^*} and ΔG_{HO^*} with a high coefficient of determination ($R^2 = 0.99$) suggests their strong linear relationship. The slope of 0.84 in the relationship of ΔG_{HO^*} vs ΔG_{HOO^*} reflects the fact that both adsorbed HO* and HOO* form a single bond between oxygen and TM, which agrees with those of metal and metal oxide surfaces^[74, 75]. For the TM@V_C systems (**Fig. 4b**), there is also a strong linear relationship between ΔG_{HOO^*} and ΔG_{HO^*} via equation $\Delta G_{\text{HOO}^*} = 0.91\Delta G_{\text{HO}^*} + 3.24$ with a high coefficient of determination ($R^2 = 0.98$). The slope of the unit in the correlated adsorption free energies of HO* vs HOO* indicates that both two intermediates form a single bond between the O atom and the TM@V_C catalyst. Herein, the overpotential (η^{OER} and η^{ORR}) as a function of four variables (ΔG_{a} , ΔG_{b} , ΔG_{c} and ΔG_{d}) can be reduced to two independent variables based on the above calculated scaling relationship as well as $\Delta G_{\text{a}} + \Delta G_{\text{b}} + \Delta G_{\text{c}} + \Delta G_{\text{d}} = 4.92$ eV (the standard Gibbs free energy of H₂O formation from O₂ and 2H₂)^[70, 75]. As shown in the follows $\Delta G_{\text{a}} = \Delta G_{\text{HO}^*}$, $\Delta G_{\text{b}} = \Delta G_{\text{O}^*} - \Delta G_{\text{HO}^*}$, $\Delta G_{\text{c}} = \Delta G_{\text{HOO}^*} - \Delta G_{\text{O}^*}$ and $\Delta G_{\text{d}} = 4.92 - \Delta G_{\text{HOO}^*}$. Thus, knowing only two descriptors, ΔG_{HO^*} and $\Delta G_{\text{O}^*} - \Delta G_{\text{HO}^*}$, is sufficient for us to describe the catalytic performance of the considered catalysts for the OER and ORR.

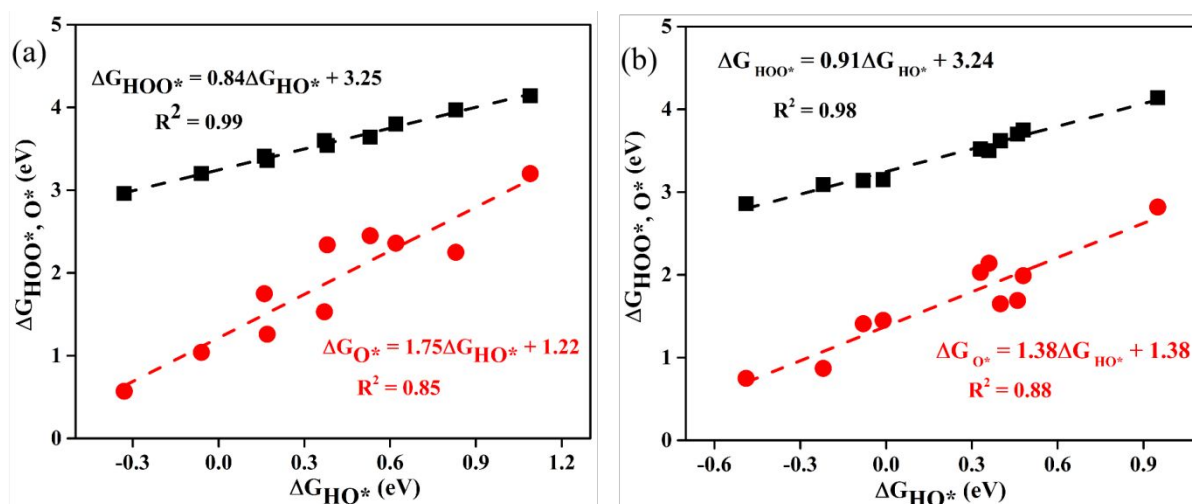


Fig. 4. The scaling relationship among the adsorption Gibbs free energies of the OER and ORR intermediates on (a) TM@V_B and (b) TM@V_C systems.

For the TM@V_B systems, we plot the two-dimensional volcano to exhibit their OER activities' trend through η^{OER} as the function of two independent descriptors ΔG_{HO^*} and $\Delta G_{\text{O}^*} - \Delta G_{\text{HO}^*}$ (**Fig. 5a**). The blue region of the two-dimensional volcano plot exhibits the highest activity area with η^{OER} reaches a minimum value of 0.11 V under the optimum condition ($\Delta G_{\text{a}} = \Delta G_{\text{b}} = \Delta G_{\text{c}} = 1.34$ eV). Among the considered TM@V_B catalysts, Co@V_B is found to be the best catalyst for OER with overpotential η^{OER} of 0.43 V followed by Rh@V_B ($\eta^{\text{OER}} = 0.49$ V) with the third steps (HOO* formation) as the rate-determining step for both catalysts. The free energy diagrams for all the intermediate states of Co@V_B and Rh@V_B systems toward OER are shown in **Fig. 6** at $U = 0$ V. Pt@V_B also exhibits good activity ($\eta^{\text{OER}} = 0.50$ V) for OER with the rate-determining step of O* formation. Notably, the calculated η^{OER} values of Co@V_B, Rh@V_B and Pt@V_B are comparable or even lower than the current best metal oxides catalysts of RuO₂ ($\eta^{\text{OER}} = 0.42$ V)^[75] and IrO₂ ($\eta^{\text{OER}} = 0.52$ V)^[74]. **Fig. 5b** represents the two-dimensional volcano showing the ORR activity trends of considered TM@V_B catalysts through η^{ORR} as the function of ΔG_{HO^*} and $\Delta G_{\text{O}^*} - \Delta G_{\text{HO}^*}$ as the independent descriptors. Under the optimal condition ($-\Delta G_{\text{a}} = -\Delta G_{\text{d}} = 0.91$ eV), the theoretical η^{ORR} is found as low as 0.32 V. The best TM@V_B catalyst for the ORR is found to be Rh@V_B with a η^{ORR} value of 0.40 V and the rate-determining step is the release of adsorbed HO*, followed by Pd@V_B ($\eta^{\text{ORR}} = 0.45$ V) with the rate-determining step of the

reduction of O_2 to HOO^* formation. Their thermodynamic limiting overpotentials are even lower than that of Pt (111) ($\eta^{ORR} = 0.48$ V)^[76]. Obviously, $Rh@V_B$ can serve as an efficient bifunctional catalyst for both OER and ORR with calculated η^{OER} of 0.49 V and η^{ORR} of 0.40 V, being able to well catalyze both OER and ORR at the same active site, respectively.

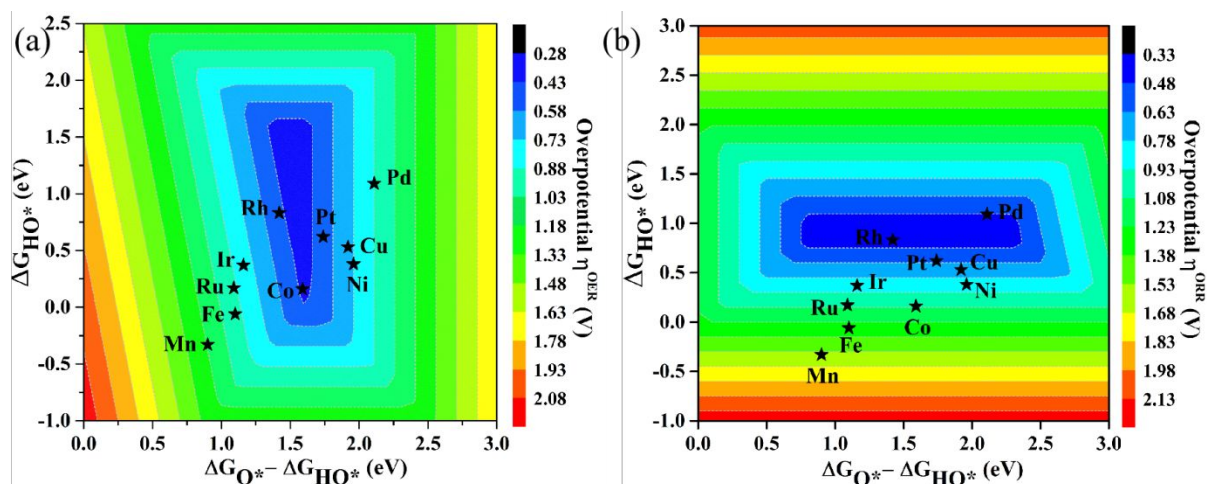


Fig. 5. Colored contour plots of (a) OER and (b) ORR activity volcanos for $TM@V_B$ systems showing the overpotentials η^{OER} and η^{ORR} as a function of adsorption Gibbs free energies of the intermediates. The color bar represents the value of η .

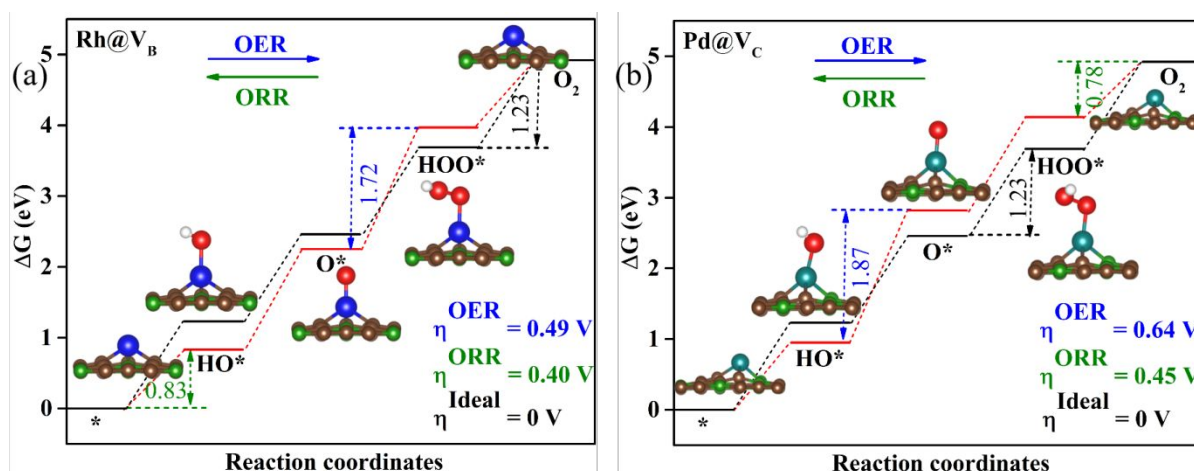


Fig. 6. Gibbs free energy diagrams of OER and ORR on (a) $Rh@V_B$ and (b) $Pd@V_C$ systems. The black and red lines are the ideal and $Rh@V_B/Pd@V_C$ Gibbs free energy diagrams, respectively. The blue and green dash lines represent the rate-limiting step for OER and ORR, respectively. The optimized configurations of adsorbed intermediates are also exhibited.

For the TM@V_C systems, we also plot the two-dimensional volcano to show the catalytic activity trend for OER/ORR through calculated overpotential $\eta^{\text{OER}}/\eta^{\text{ORR}}$ as a function of two independent descriptors ΔG_{HO^*} and $\Delta G_{\text{O}^*} - \Delta G_{\text{HO}^*}$ (**Fig. 7**). Under the optimum condition ($\Delta G_{\text{a}} = \Delta G_{\text{b}} = \Delta G_{\text{c}}$), the maximum free energy change during OER process is only 1.55 eV, indicating that the minimum η^{OER} is 0.32 V. The best catalyst for the OER among the considered TM@V_C catalysts is found to be Ni@V_C with the calculated η^{OER} value of 0.47 V and the corresponding rate-limiting step is the O* formation. Pt@V_C, Co@V_C, Rh@V_C, and Ir@V_C catalysts also exhibit good catalytic activity for the OER with the calculated η^{OER} of 0.53, 0.54, 0.55 and 0.55 V, respectively, and the corresponding rate-limiting step is HOO* formation, HOO* formation, O* formation and desorption of O₂. **Fig. 7b** shows the calculated theoretical two-dimensional volcano for the ORR occurring on all the considered TM@V_C systems. As discussed above, under the optimal condition ($-\Delta G_{\text{a}} = -\Delta G_{\text{d}}$), the theoretical η^{ORR} is only 0.35 V. The calculated two-dimensional volcano shows that Pd@V_C as the most active ORR catalyst with the η^{ORR} value of 0.45 V and the release of adsorbed HO* is the rate-limiting step (**Fig. 6b**).

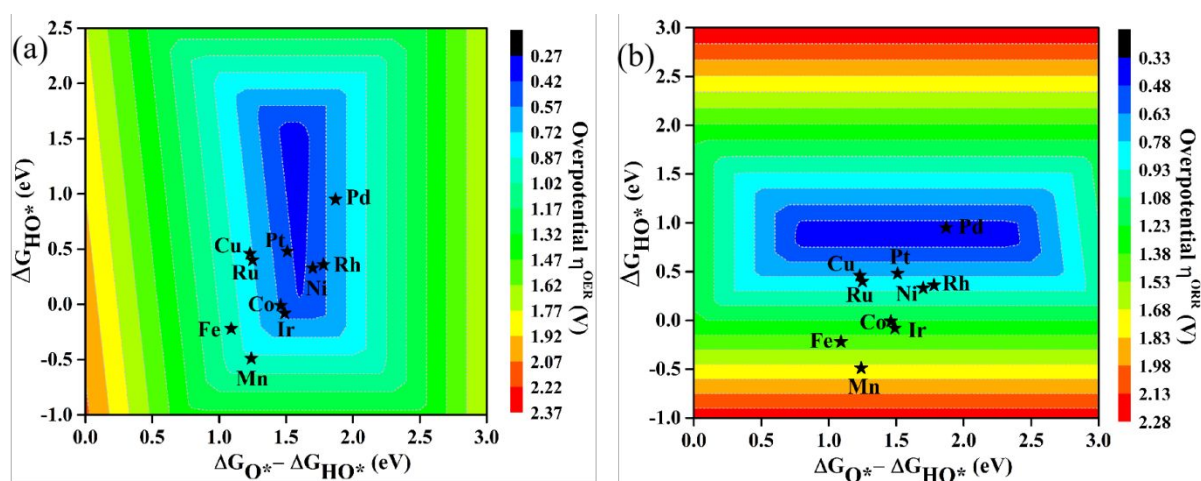


Fig. 7. Colored contour plots of (a) OER and (b) ORR activity volcanos for TM@V_C systems showing the overpotentials η^{OER} and η^{ORR} as a function of adsorption Gibbs free energies of the intermediates. The color bar represents the value of η .

In addition to the high-activity of the active site toward OER and ORR, it is vital to investigate the stability of the catalyst. Previous results have suggested that the main issue of the high-activity atomically dispersed active site is demetalation, that's due to the proton

attack of the active region, which can lead to the degradation of catalyst activity^[77-79]. Thus, we simulated the reaction free energy (ΔG_{diss}) to evaluate the stability of metal active center against dissolution by the following equation^[72]: $\text{TM@V} + n\text{H}^+ \rightarrow n\text{H@V} + \text{TM}^{n+}$. Where n refers to the oxidation state for the TM atom, $n\text{H@V}$ refers to the $V_{\text{B}}/V_{\text{C}}$ monolayer with TM vacancy adsorbed by n number of hydrogen atoms (**Fig. S3**). The dissolution energy can be calculated as: $\Delta G_{\text{diss}} = G_{(n\text{H@V})} + G_{(\text{TM}^{n+})} - G_{(\text{TM@V})} - nG_{(\text{H}^+)}$. Here, $G_{(n\text{H@V})}$ and $G_{(\text{TM@V})}$ can be obtained directly from DFT calculation, and $\Delta G_{(\text{H}^+)} = 0.5 \times G_{(\text{H}_2)} - \ln 10 \times kT \times \text{pH} = 0.5 \times [E_{(\text{H}_2)} + \text{ZPE}_{(\text{H}_2)} - \text{TS}_{(\text{H}_2)}] - \ln 10 \times kT \times \text{pH}$. Here, the TS value for H_2 gas phase at 298K is taken as 0.41 eV, and the ZPE value for H_2 gas phase is 0.26 eV^[12]. As for $G_{(\text{TM}^{n+})}$, we take the experimental ion formation of TM^{n+} , which is defined as: $\Delta G_{(\text{TM}^{n+})} = G_{(\text{TM}^{n+})} - G_{(\text{TM, bulk})}$. Thus, we can know: $G_{(\text{TM}^{n+})} = \Delta G_{(\text{TM}^{n+})} + G_{(\text{TM, bulk})}$, where $G_{(\text{TM, bulk})}$ is calculated directly and $\Delta G_{(\text{TM}^{n+})}$ is taken from literature^[80] and listed in **Table S5** and **S6**. Based on the above approach, the dissolution energy at pH = 0 condition, $\Delta G_{\text{diss}}(0)$, can be calculated and shown in **Fig. 8**. We can conclude that Rh-, Pd-, Ir-, and Pt-doped on V_{C} and V_{B} catalysts are stable against dissolution at the pH = 0 condition. The negative values of $\Delta G_{\text{diss}}(0)$ for other TMs suggest that they are unstable against dissolution. Meanwhile, with the increase of the pH value, the $\Delta G_{\text{diss}}(\text{pH})$ also increases, thus, there exist a critical pH value, above which the TM@V catalyst will be stable. The critical pH value can be evaluated by $\text{pH}_{\text{min}} = -\Delta G_{\text{diss}}(0) / (n \times 0.0591)$ (**Table S5** and **S6**). Therefore, when the system is sufficiently alkali, the catalyst will always be stable against dissolution, and Rh@V, Pd@V, Ir@V, and Pt@V are stable even at acidic condition.

To further evaluate the dynamic stability of Rh@ V_{B} against agglomeration, the diffusion barrier of doped Rh on V_{B} was calculated. As shown in **Fig. S4**, the diffusion of adsorbed Rh atom from the vacancy adsorption site to its neighboring hollow site needs to overcome an energy barrier of 5.52 eV, suggesting that the adsorbed Rh atom on V_{B} hardly diffuses to form clusters. Therefore, as discussed above, Rh@ V_{B} is indeed a highly efficient and stable single-atom catalyst for both OER and ORR.

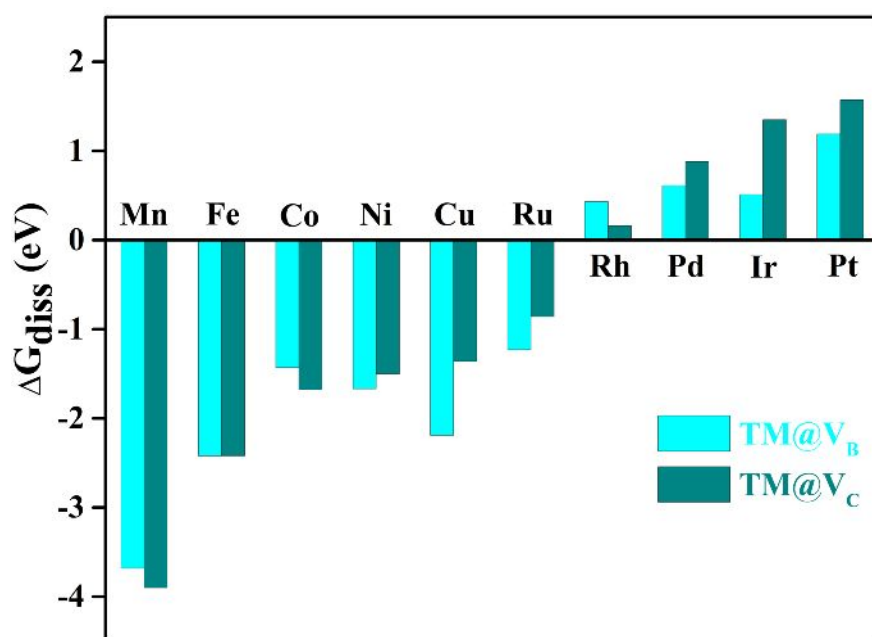


Fig. 8. Calculated reaction free energy shows the stability of TM@V_B and TM@V_C catalysts against TM atom dissolution at pH = 0 condition.

Conclusion

In summary, by using the computational screening method, we have systematically screened a series of single transition metal atoms doped on point defect BC₃ monolayer as high-activity and stable single atom catalyst for both OER and ORR. It was found that with the increase of the *d*-electron number of the doped TM atom on defective BC₃ monolayer, the *d*-band center moves to lower energy level that leads to the weaker interaction strength between the intermediates and TM active site. Thus, the optimal catalyst for OER and ORR can be selected by tuning the doped TM element. According to the volcano plots of the OER and ORR, the best catalyst for OER among the studied TM@V_B catalysts is Co@V_B with η^{OER} of 0.43 V followed by Rh@V_B (η^{OER} =0.49 V), and for ORR, the best catalyst is Rh@V_B with η^{ORR} of 0.40 V followed by Pd@V_B (η^{ORR} =0.45 V). While, among the considered TM@V_C catalysts, Ni@V_C (η^{OER} =0.47 V) exhibits the highest activity toward OER followed by Pt@V_C (η^{OER} =0.53 V), and for ORR, the best catalyst is Pd@V_C with the calculated overpotential η^{ORR} of 0.45 V. It should be pointed that the well dispersed Rh@V_B can exhibit high activity for both OER and ORR, importantly, it can remain stable against dissolution at pH=0 condition. Thus, Rh@V_B can serve as efficient, stable and low-cost single metal atom

catalyst toward both OER and ORR. Our results shed light on BC₃-based material as the efficient and stable OER/ORR catalyst and offer us a useful guideline to screen the metal active site of single atom catalyst on 2D materials.

Conflicts of interest

There are no conflicts to declare.

Acknowledgments

This work was supported by the Assistant Secretary for Energy Efficiency and Renewal Energy of the U.S. Department of Energy under the Hydrogen Generation program. This theoretical work used the resources of the National Energy Research Scientific Computing Center (NERSC) that is supported by the Office of Science of the U. S. Department of Energy. We are grateful to the Chinese Scholarship Council (CSC) for providing the Ph.D. scholarship.

References

- [1] Y. Jiao, Y. Zheng, M. Jaroniec, S.Z. Qiao, *Chem. Soc. Rev.* 44 (2015) 2060-2086.
- [2] C.G. Morales-Guio, L.A. Stern, X. Hu, *Chem. Soc. Rev.* 43 (2014) 6555-6569.
- [3] G.S. Liu, S.J. You, Y. Tan, N.Q. Ren, *Environ. Sci. Technol.* 51 (2017) 2339-2346.
- [4] E.A. Paoli, F. Masini, R. Frydendal, D. Deiana, C. Schlaup, M. Malizia, T.W. Hansen, S. Horch, I.E.L. Stephens, I. Chorkendorff, *Chem Sci.* 6 (2015) 190-196.
- [5] Z.W.Q. J. Rossmeisl, H. Zhu, G.J. Kroes, J.K. Nørskov, *J. Electroanal. Chem.* 607 (2007) 83-89.
- [6] N.M. Markovic, T.J. Schmidt, V. Stamenkovic, P.N. Ross, *Fuel Cells* 2 (2001) 105-116.
- [7] X.Q. Huang, Z.P. Zhao, L. Cao, Y. Chen, E.B. Zhu, Z.Y. Lin, M.F. Li, A.M. Yan, A. Zettl, Y.M. Wang, X.F. Duan, T. Mueller, Y. Huang, *Science* 348 (2015) 1230-1234.
- [8] J. Li, G. Zheng, *Adv. Sci.* 4 (2017) 1600380.
- [9] T. Sun, B. Tian, J. Lu, C. Su, *J. Mater. Chem. A* 5 (2017) 18933-18950.
- [10] G.P. Gao, E.R. Waclawik, A.J. Du, *J. Catal.* 352 (2017) 579-585.
- [11] Y.N. Zhou, G.P. Gao, Y. Li, W. Chu, L.W. Wang, *Phys. Chem. Chem. Phys.* 21 (2019) 3024-3032.
- [12] Y.N. Zhou, G.P. Gao, J. Kang, W. Chu, L.W. Wang, *J. Mater. Chem. A* 7 (2019) 12050.
- [13] X.P. Gao, Y.N. Zhou, Y.J. Tan, B.W. Yang, Z.W. Cheng, Z.M. Shen, *Int. J. Hydrogen Energy* 44 (2019) 14861-14868.
- [14] X.P. Gao, Y.N. Zhou, Y.J. Tan, B.W. Yang, Z.W. Cheng, Z.M. Shen, J.P. Jia, *Appl. Surf. Sci.* 473 (2019) 770-776.
- [15] B.T. Qiao, A.Q. Wang, X.F. Yang, L.F. Allard, Z. Jiang, Y.T. Cui, J.Y. Liu, J. Li, T. Zhang, *Nat. Chem.* 3 (2011) 634-641.

- [16] X.F. Yang, A.Q. Wang, B.T. Qiao, J. Li, J.Y. Liu, T.Zhang, 46 (2013) 1740-1748.
- [17] K.S. Novoselov, A.K. Geim, S.V. Morozov, D. Jiang, Y. Zhang, S.V. Dubonos, I.V. Grigorieva, A.A. Firsov, *Science* 306 (2004) 666-669.
- [18] Q. Tang, Z. Zhou, *Prog. Mater. Sci.* 58 (2013) 1244-1315.
- [19] M.S. Xu, T. Liang, M.M. Shi, H.Z. Chen, Graphene-like two-dimensional materials, *Chem. Rev.* 113 (2013) 3766-3798.
- [20] C.Z. Zhu, S.F. Fu, Q.R. Shi, D. Du, Y.H. Lin, *Angew. Chem. Int. Ed.* 56 (2017) 13944-13960.
- [21] B. Bayatsarmadi, Y. Zheng, A. Vasileff, S.Z. Qiao, *Small* 13 (2017) 1700191.
- [22] J.P. Paraknowitsch, A. Thomas, *Energy Environ. Sci.* 6 (2013) 2839.
- [23] H.B. Yang, J.W. Miao, S.F. Hung, J.Z. Chen, H.B. Tao, X.X. Wang, L.P. Zhang, R. Chen, J.J. Gao, H.M. Chen, L.M. Dai, B. Liu, *Sci. Adv.* 2 (2016) 1501122.
- [24] S. Back, J. Lim, N.Y. Kim, Y.H. Kim, Y. Jung, *Chem. Sci.* 8 (2017) 1090-1096.
- [25] T.V. Vineesh, M.P. Kumar, C. Takahashi, G. Kalita, S. Alwarappan, D.K. Pattanayak, T.N. Narayanan, *Adv. Energy Mater.* 5 (2015) 1500658.
- [26] R. Shang, S.N. Steinmann, B.Q. Xu, P. Sautet, *Catal. Sci. Technol.* 10 (2020) 1006-1014.
- [27] Y.Y. Huang, Y.Q. Wang, C. Tang, J. Wang, Q. Zhang, Y.B. Wang, J.T. Zhang, *Adv Mater.* 31 (2019) 1803800.
- [28] C. Tang, H.F. Wang, X. Chen, B.Q. Li, T.Z. Hou, B.S. Zhang, Q. Zhang, M.M. Titirici, F. Wei, *Adv Mater.* 28 (2016) 6845-6851.
- [29] Y. Zheng, Y. Jiao, Y. Zhu, Q. Cai, A. Vasileff, L.H. Li, Y. Han, Y. Chen, S.Z. Qiao, *J. Am. Chem. Soc.* 139 (2017) 3336-3339.
- [30] B.Y. Xia, Y. Yan, N. Li, H.B. Wu, X.W. Lou, X. Wang, *Nat. Energy.* 1 (2016) 15006.
- [31] W.P. Yang, X.X. Li, Y. Li, R.M. Zhu, H. Pang, *Adv. Mater.* 31 (2019) 1804740.
- [32] J.X. Gu, S. Magagula, J.X. Zhao, Z.F. Chen, *Small Methods*, 3 (2019) 1800550.
- [33] X.P. Gao, Y.N. Zhou, Y.J. Tan, S. Liu, Z.W. Cheng, Z.M. Shen, *Appl. Surf. Sci.* 492 (2019) 8-15.
- [34] X.Y. Guo, S.R. Lin, J.X. Gu, S.L. Zhang, Z.F. Chen, S.P. Huang, *ACS Catal.* 9 (2019) 11042-11054.
- [35] Y.N. Zhou, G.P. Gao, W. Chu, L.W. Wang, *Nanoscale Adv.* 2 (2020) 710-716.
- [36] X.Y. Luo, J.H. Yang, H.Y. Liu, X.J. Wu, Y.C. Wang, Y.M. Ma, S.H. Wei, X.G. Gong, H. Xiang, *J. Am. Chem. Soc.* 133 (2011) 16285-16290.
- [37] L.J. Yang, S.J. Jiang, Y. Zhao, L. Zhu, S. Chen, X.Z. Wang, Q. Wu, J. Ma, Y.W. Ma, Z. Hu, *Angew. Chem. Int. Ed.* 50 (2011) 7132-7135.
- [38] H. Yanagisawa, T. Tanaka, Y. Ishida, M. Matsue, E. Rokuta, S. Otani, C. Oshima, *Phys. Rev. Lett.* 93 (2004) 177003.
- [39] B. Ozdemir, V. Barone, *Comput. Mater. Sci.* 109 (2015) 248-252.
- [40] Q. Wang, L.Q. Chen, *Phys. Rev. B* 54 (1996) 2271-2275.
- [41] A.S. Mikhaylushkin, X.W. Zhang, A. Zunger, *Phys. Rev. B* 87 (2013) 094103-094109.
- [42] Y.Y. Liu, V.I. Artyukhov, M.J. Liu, A.R. Harutyunyan, B.I. Yakobson, *J. Phys. Chem. Lett.* 4 (2013) 1737-1742.
- [43] C. Ling, F. Mizuno, *Phys. Chem. Chem. Phys.* 16 (2014) 10419-10424.
- [44] Y.N. Tang, H.D. Chai, H.W. Zhang, W.G. Chen, W.Q. Zhang, X.Q. Dai, *Phys. Chem. Chem. Phys.* 20 (2018) 14040-14052.
- [45] T. Hussain, D.J. Searles, K. Takahashi, *J. Phys. Chem. A* 120 (2016) 2009-2013.
- [46] X.Q. Lin, J. Ni, *J. Appl. Phys.* 111 (2012) 034309.
- [47] S. Behzad, *Surf. Sci.* 665 (2017) 37-42.

- [48] J.Z. Zhu, Y.C. Zhao, M. Zulfiqar, S.M. Zeng, J. Ni, *Phys. Lett. A* 382 (2018) 1395-1400.
- [49] F. Banhart, J. Kotakoski, A.V. Krasheninnikov, *ACS Nano* 5 (2011) 26-41.
- [50] H.I. Rasool, C. Ophus, A. Zettl, *Adv. Mater.* 27 (2015) 5771-5777.
- [51] C. Rivera-Carcamo, P. Serp, *ChemCatChem* 10 (2018) 5058-5091.
- [52] G. Kresse, J. Furthmuller, *Comput. Mater. Sci.* 6 (1996) 15-50.
- [53] G. Kresse, *Phys. Rev. B* 54 (1996) 11169-11186.
- [54] P.E. Blochl, *Phys. Rev. B* 50 (1994) 17953-17979.
- [55] J.P. Perdew, M. Ernzerhof, K. Burke, *J. Chem. Phys.* 105 (1996) 9982-9985.
- [56] J.P. Perdew, K. Burke, M. Ernzerhof, *Phys. Rev. Lett.* 7 (1996) 3865-3868.
- [57] S. Grimme, J. Antony, S. Ehrlich, H. Krieg, *J. Chem. Phys.* 132 (2010) 154104.
- [58] H.J. Monkhorst, J.D. Pack, *Phys. Rev. B* 13 (1976) 5188-5192.
- [59] W. Tang, E. Sanville, G. Henkelman, *J. Phys. Condens. Matter.* 21 (2009) 084204.
- [60] G. Henkelman, B.P. Uberuaga, H. Jonsson, *J. Chem. Phys.* 113 (2000) 9901-9904.
- [61] G. Henkelman, A. Arnaldsson, H. Jonsson, *Comput. Mater. Sci.* 36 (2006) 354-360.
- [62] K. Mathew, R. Sundararaman, K. Letchworth-Weaver, T.A. Arias, R.G. Hennig, *J. Chem. Phys.* 140 (2014) 084106.
- [63] Y. Ding, Y.L. Wang, J. Ni, *J. Phys. Chem. C*, 114 (2010) 12416-12421.
- [64] S.Y. Liu, S.Y. Liu, D.J. Li, H.L. Dang, Y.D. Liu, S. Xue, W.H. Xue, S.S. Wang, *Phys. Rev. B* 88 (2013) 115434-115439.
- [65] Y.C. Ma, P.O. Lehtinen, A.S. Foster, R.M. Nieminen, *New J. Phys.* 6 (2004) 68.
- [66] A.A. El-Barbary, R.H. Telling, C.P. Ewels, M.I. Heggie, P.R. Briddon, *Phys. Rev. B* 68 (2003) 144107-144114.
- [67] Y.N. Zhou, W. Chu, F.L. Jing, J. Zheng, W.J. Sun, Y. Xue, *Appl. Surf. Sci.* 410 (2017) 166-176.
- [68] M. Mavrikakis, B. Hammer, J. K. Nørskov, *Phys. Rev. Lett.* 81 (1998) 2819-2822.
- [69] B. Hammer, J.K. Nørskov, *Adv. Catal.* 45 (2000) 71-129.
- [70] J.K. Nørskov, J. Rossmeisl, A. Logadottir, L. Lindqvist, *J. Phys. Chem. B* 2004, 108, 17886-17892.
- [71] J.K. Nørskov, T. Bligaard, A. Logadottir, J.R. Kitchin, J.G. Chen, S. Pandalov, U. Stimming, *J. Electrochem. Soc.* 152 (2005) 23-26.
- [72] F. Calle-Vallejo, J.I. Martínez, J.M. García-Lastra, E. Abad, M.T.M. Koper, *Surf. Sci.* 607 (2013) 47-53.
- [73] M.T.M. Koper, *J. Electroanal. Chem.* 660 (2011) 254-260.
- [74] J. Rossmeisl, A. Logadottir, J.K. Nørskov, *Chem. Phys.* 319 (2005) 178-184.
- [75] I.C. Man, H.Y. Su, F. Calle-Vallejo, H.A. Hansen, J.I. Martínez, N.G. Inoglu, J. Kitchin, T.F. Jaramillo, J.K. Nørskov, J. Rossmeisl, *ChemCatChem* 3 (2011) 1159-1165.
- [76] J. Greeley, I.E. Stephens, A.S. Bondarenko, T.P. Johansson, H.A. Hansen, T.F. Jaramillo, J. Rossmeisl, I. Chorkendorff, J.K. Nørskov, *Nat. Chem.* 1 (2009) 552-556.
- [77] J.C. Meier, C. Galeano, I. Katsounaros, J. Witte, H.J. Bongard, A.A. Topalov, C. Baldizzone, S. Mezzavilla, F. Schuth, K.J.J. Mayrhofer, *Beilstein J. Nanotechnol.* 5 (2014) 44-67.
- [78] S. Gupta, D. Tryk, I. Bae, W. Aldred, E. Yeager, *J. Appl. Electrochem.* 19 (1989) 19-27.
- [79] U. Martinez, S. Komini Babu, E.F. Holby, H.T. Chung, X. Yin, P. Zelenay, *Adv Mater.* (2019) 1806545.
- [80] J. Greeley, J.K. Nørskov, *Electrochim. Acta* 52 (2007) 5829-5836.